Interfacial stabilization for inverted perovskite solar cells with long-term stability

Wei Chen[1,2],† Bing Han[1]† Qin Hu,[3,8]†, Meng Gu,[1] Yudong Zhu,[1] Wenqiang Yang,[4] Yecheng Zhou,[5] Deying Luo,[4] Fang-Zhou Liu,[2] Rui Cheng,[6] Rui Zhu,[4] Shien Ping Feng,[6] Aleksandra B. Djurišić,[2]* Thomas P. Russell[3,7]* and Zhubing He[1]*

[1]Department of Materials Science and Engineering, Shenzhen Key Laboratory of Full Spectral Solar Electricity Generation (FSSEG), Southern University of Science and Technology, No. 1088, Xueyuan Rd., Shenzhen, 518055, Guangdong, P.R. China.

[2]Department of Physics, The University of Hong Kong, Pokfulam, Hong Kong SAR.

[3]Materials Sciences Division, Lawrence Berkeley National Laboratory, Berkeley, California 94720, USA.

[4]State Key Laboratory for Artificial Microstructure and Mesoscopic Physics, Department of Physics, Peking University, Beijing 100871, China.

[5]Department of Physics, Southern University of Science and Technology, No. 1088, Xueyuan Rd., Shenzhen, 518055, Guangdong, P.R. China.

[6]Department of Mechanical Engineering, The University of Hong Kong, Pokfulam, Hong Kong SAR.

[7]Department of Polymer Science and Engineering, University of Massachusetts, Amherst, Massachusetts 01003, United States.

[8]School of Microelectronics, University of Science and Technology of China, Hefei, Anhui 230026, China

[†]These authors contributed to this work equally.

Abstract:

Perovskite solar cells (PSCs) commonly exhibit significant performance degradation due to ion migration through the top charge transport layer and ultimately metal electrode corrosion. Here, we demonstrate an interfacial management strategy using a boron chloride subphthalocyanine (Cl_6SubPc)/fullerene electron-transport layer, which not only passivates the interfacial defects in the perovskite, but also suppresses halide diffusion as evidenced by multiple techniques, including visual element mapping by electron energy loss spectroscopy. As a result, we obtain inverted PSCs with an efficiency of 22.0% (21.3% certified), shelf life of 7000 hours, T_{80} of 816 h under damp heat stress (compared to less than 20 h without Cl_6SubPc), and initial performance retention of 98% after 2000 hours at 80 ºC in inert environment, 90% after 2034 h of illumination and MPP tracking in ambient for encapsulated devices and 95% after 1272 h outdoor testing ISOS-O-1. Our strategy and results pave a new way to move PSCs forward to their potential commercialization solidly.

Keywords: Interfacial stabilization; inverted perovskite solar cells; long-term stability; NiO; halide ions diffusion.

1. Introduction

Metal halide perovskite solar cells (PSCs) have exhibited significant progress in terms of both conversion efficiency and stability in recent years [1-4]. However, the device stability is not sufficient for the commercialization, and, hence, is more crucial than conversion efficiency at present [1]. Whether conventional *n-i-p* or inverted *p-i-n* devices are used, PSCs commonly exhibit degradation when exposed to moisture, ambient atmosphere, heat, and electric bias [5, 6]. The degradation initiates from defect sites near the surfaces unpon exposure to light, moisture, oxygen, and heat, and these defects also initiate ion migration, resulting in reactions of the perovskite (PVK) at the charge transporting interfaces and the electrodes [5, 7].

Of the different device architectures, inverted PSCs are of particular interest, since the absence of doped organic charge transport layer on top of the perovskite enables superior thermal stability in comparison to conventional devices [6, 8-10], and high stability under combined light and heat stressing [6] and thermal cycling. In addition, they also exhibit improved stability under reverse bias compared to conventional devices [11-16]. It is well known that the PVK/charge transport layer, namely hole transport layer (HTL) or electron transport layer (ETL) dominate conversion efficiency and stability of devices mainly by affecting interfacial defect density and ions diffusion [17-19]. In an inverted device structure, the top PVK/ETL interface is expected to significantly influence the device stability due to its effect on moisture and oxygen penetration into the perovskite and halide ion diffusion to the electrode. It is well recognized that inverted PSCs with commonly used

fullerene-based ETLs not only exhibit significant interfacial recombination losses [17-20], but also have susceptibility to the oxygen and moisture ingress into the devices [18, 21-24]. In addition, their thermal stability is limited by the aggregation of fullerene acceptor, which leads to the deterioration of contact between PVK and ETL [21]. More importantly, volatile perovskite decomposition products readily diffuse through the fullerene-based layer, exacerbating PVK and electrode degradation, since almost all metals react with PVK decomposition products, and leading to shunting at low reverse bias voltages [25-27].

Therefore, interfacial stabilization at the interface of PVK/ETL is crucial for achieving both high efficiencies and long-term stabilities in inverted *p-i-n* PSCs. While the performance improvements have been demonstrated by various approaches [18, 28-30], including the use of different inorganic [17, 31] or organic [21, 32] interfacial layers between PVK and C_{60}, further performance improvements are still needed to bring these devices closer to commercialization. Here we use a boron chloride subphthalocyanine (Cl_6SubPc)/fullerene ETL to simultaneously reduce the interfacial defect density and hinder ion migration, resulting in power conversion efficiencies of 22.0% (certified 21.3 %), a shelf life of 7000 hours, T_{80} of 816 h under damp heat stress, and performance retention of 98% after 2000 hours at 80 ^{o}C in inert environment, and 95% after 1200 h outdoor testing (first outdoor performance test for inverted devices). Dramatic inhibition of the iodide diffusion, as evidenced by multiple experimental techniques can be attributed to the unique properties of Cl_6SubPc, forms strong Pb-Cl bonds, contributing to defect passivation, and has

strong interactions with iodine, that effectively suppresses ion migration and electrode corrosion even under extreme conditions of reverse bias under illumination.

2. Experimental

2.1 Materials: N,N-dimethylformamide (DMF), dimethyl sulfoxide (DMSO), chlorobenzene (CB), Cesium iodide (CsI) were purchased from Sigma-Aldrich. Lead (II) iodide (PbI_2) and lead (II) bromide ($PbBr_2$) were purchased from TCI. Methylammonium bromide (MABr), formamidinium Iodide (FAI) and phenethylammonium Iodide (PEAI) were purchased from GreatCell Solar Ltd. Cl_6SubPc and C_{60} were obtained from Daeyeon Chemicals Co.,Ltd. All materials above were used as received.

Device fabrication. Perovskite solar cells (PVSCs) with *p-i-n* structure were fabricated following a configuration of ITO/HTL/perovskite/ETLs/BCP/electrodes. ITO glass was cleaned by sequentially washing with detergent, deionized water, Acetone, and isopropanol. The substrates were dried with N_2 and cleaned by UV ozone for 15 min. Cu:NiO_x HTLs were spin coated on the clean ITO substrates according to our previous reports [33-35]. The CsFAMA mixed perovskite layers were fabricated according to our previously reported one-step antisolvent method [35]. In details, the perovskite precursor solution was prepared by mixing PbI_2, $PbBr_2$, FAI and MABr in DMF/DMSO (v/v:4/1) where the mole concentration of PbI_2 was kept at 1.1 M, and the mole ratio of I/Br and FA/MA were maintained at 0.85/0.15. After stirring 1 hour at 60 ºC, 35 µl of CsI (2 M in DMSO) was added and stirred another 1 hour. The perovskite films were deposited on HTLs with 4000 rpm for 35s, during spinning, 300 µL CB was used as antisolvent 25 s prior to the end of the spinning process. Then the perovskite films were annealed at 100 ºC for 60mins. After cooling

down to room temperature, 100 µl PEAI solutions (2mg/ml in IPA) were quickly dropped on CsFAMA mixed perovskite and spin coated with 5000 rpm for 45 s and annealed at 110 ºC for 10 min. The substrates were then transferred into high vacuum thermal evaporator where the ETLs Cl_6SubPc (8 nm) and C_{60} (20 nm), BCP (8 nm) and metal electrode (Ag (120 nm) or Cu (120 nm) or Au (80 nm)) were subsequently evaporated. The active area was defined with a shadow mask.

2.2 Device and film characterization. *J-V* measurements were carried out using a Keithley 2400 source meter in ambient environment at ~23 ºC and ~45% RH. The devices were measured both in reverse scan (1.2 V→-0.2 V, step 0.01 V) and forward scan (-0.2 V→1.2 V, step 0.01 V) with 10 ms delay time. Illumination was provided by an Oriel Sol3A solar simulator with AM1.5G spectrum and light intensity of 100 mW/cm^2, which was calibrated by a standard KG-5 Si diode. During I-V measurement, optical aperture mask (8.939 mm^2) was used to verify the accurate the cell area. EQE measurements for devices were conducted with an Enli-Tech (Taiwan) EQE measurement system. AFM-based experiments were measured in ambient condition (25 ºC and 38% RH) with Atomic Force Microscope (MFP-3D-BIO, Asylum Research, USA). Top-view morphology was analyzed by TESCAN MIRA3. A FEI Helios Nanolab 600i dual beam focus ion beam/field emission gun-scanning electron microscope (FIB/FEGSEM) was used to prepare cross-section for STEM imaging and analysis. FEI Talos transmission electron microscope (TEM) with Super-X EDX was employed to acquire the STEM-EDX data with STEM-HAADF (high-angle annular dark field) mode. STEM-EELS was carried out on a double Cs-corrected TEM (Titan Themis 60-300kV) performed by a Gatan cooling holder at the liquid nitrogen temperature. For HR-TEM image, the prepared FIB lamina was then immediately dropped in liquid nitrogen and transferred by a Cryo-transfer loader

into cryogenic chamber of Titan Krios cryo-TEM (Thermo Fisher Scientific Ltd.). The cryo-TEM images were acquired using a low electron dose detector (Falcon, Thermo Fisher Scientific Ltd.). The dose rate for each Cryo-TEM image is controlled to below ~50 e $Å^{-2}$ S^{-1} for high resolution images and 1.5 e $Å^{-2}$ S^{-1} for the low magnification images, correspondingly. To decrease the dose rate, continuous 79 frames were acquired in 2s and were integrated into one image with drift-correction aligned. The operation voltage of electron beam is 300 kV. Depth profiling data were obtained with ToF-SIMS 5 system from ION-TOF. The X-ray diffraction patterns were obtained using a BRUKER ECO D8 series. Time resolved PL spectra were measured using a Spectrofluorometer (FS5, Edinburgh instruments) and 405 nm pulsed laser was used as excitation source for the measurement. UPS and XPS measurements were performed on an ESCALAB 250Xi, Thermo Fisher (by using Al Kα x-ray source) under high vacuum (10^{-9} mbar). The XPS spectra were calibrated by the binding energy of C 1s. Mott–Schottky and density of states characteristics were analyzed with a Zahner IM6e electrochemical station (Zahner, Germany) in ambient environment of 25 ºC and 38% RH.

2.3 Grazing-incidence Wide-Angle X-ray Scattering (GIWAXS): GIWAXS experiments were performed at beamline 7.3.3 of the Advanced Light Source (ALS), Lawrence Berkeley National Laboratory (LBNL). The X-ray energy was 10 keV, and the two-dimensional (2D) scattering patterns were acquired with a Dectris Pilatus 2M CCD detector (172 µm x 172 µm pixel size). Grazing incidence angles of 0.5º was collected to explore the crystal structure. All the perovskite films were deposited on Si/Cu:NiO_x substrates, while the Cl_6SubPc and C_{60} films were deposited on Si substrates. All the samples were imaged at ambient temperature in an enclosed

Helium box to ensure minimize background scattering. Data analysis was performed using IGOR Pro software with the Nika package.

2.4 Device stability. For the maximum power point (MPP) tracking test, the encapsulated device was fixed at the V_{mpp} and the current density variation under ambient environment (~23.5 ºC, 34% RH) was recorded without controlling the device temperature. For thermal stability evaluation, the devices were stored in an inert environment (O_2 < 0.1ppm, H_2O < 0.1ppm) at room temperature and/or 80 ºC. The devices were kept under dark except during the I-V measurement, and the I-V curves were recorded in certain time intervals. For damp heat tests, the devices were stored at environmental chamber with fixed temperature and humidity (85 ºC and 85% RH) except during the I-V measurement. For outdoor tests, the devices were mounted on sample holder at 22º angle with the front side oriented towards the equator, located on the rooftop without any blocking or shading of the sunshine. The devices for damp heat, outdoor and MPPT in ambient environment under illumination tests were carefully encapsulated with desiccant coverage in the cell area and epoxy edge sealing following our previous encapsulation recipe [36].

2.5 Theoretical calculations: DFT calculations: In order to investigate how the molecules interact with perovksite layer and improve its stability, molecular dynamics simulations were performed by Viena *Ab initio* Simulation Package 5. 4 (VASP), which has been implemented with projector augmented wave (PAW) method. The exchange-correlation of generalized gradient approximation (GGA) was described by the Perdew–Burke–Ernzerhof (PBE) functional revised for solid, which gives lattice constant close to experiments [37]. The final adsoprtion configurations were relaxed from structures obtained from an *ab initio* molecular dynamics (NVT ensemble , with Γ point) with a time step of 1 fs at 500 K for 3 ps. An energy cutoff of 450 eV was

employed. At least two possible adsorption configurations were achieved. In both cases, two Cl ions of the molecules are bonded with Pb ions in perovskite, indicating strong interaction between the perovskite and Cl_6SubPc. The binding energies are calculated to be -1.24 eV for the configurations. Compared to the binding energy (-0.11 eV) of C60, the bond between Pb ions and Cl_6SubPc is much stronger. For the calculation of the binding energy between the 2D PEA^+ cation (PEA-PEA), and the PEA^+ with Cl_6SubPc molecule (PEA-Cl_6SubPc-PEA), structure optimization and energy calculations were performed by VASP 5.4.4 [38, 39], which is implemented with the projector-augmented wave potentials. PBE functional was used to describe the exchange correlation. A cut off energy of Plane-wave basis sets is set as 550 eV. Due to the big size of molecules, the used surface is very large (19.08×19.14 $Å^2$) hence only Γ-point was used to relax the structure and a Γ-point centered 3×3×1 k-mesh was used for static energy calculations.

3. Results and discussion

3.1 Device performance of the inverted PSCs with different ETLs.

Phthalocyanine and porphyrin have excellent thermal and photochemical stability and have been used in different types of solar cells, including PSCs [40] and organic photovoltaics OPVs [41]. Phthalocyanine- and porphyrin-related molecules exhibit one intriguing aspect, namely their high iodine adsorption capacity and general capability of adsorption of various guest molecules owing to their cloud of π electrons [42]. This aspect of phthalocyanine-related molecules has been little explored in PSCs, but potentially offers a route to inhibit ion migration and/or diffusion of perovskite decomposition products through the ETL, protecting the electrode from corrosion. Thus, we investigated the use of a chlorinated macrocyclic molecule, Cl_6SubPc,

which has been previously used as an acceptor in OPVs [40]. The chemical structure of Cl_6SubPc and the device architecture of *p-i-n* planar PSCs are shown in **Fig. 1a and 1b**. We use inorganic Cu doped NiO_x nanoparticles as the HTL and C_{60} as the ETL [34], and a Cs^+, formamidinium (FA^+) and methylammonium (MA^+) (CsFAMA) cations mixed perovskite [25, 43] as the active layer. We investigated both CsFAMA perovskites, labeled as 3D PVK, and CsFAMA perovskites with the surface treated with phenyl ethyl-ammonium iodide (PEAI) solution, labeled as 3D/2D PVK (for experimental details, see Methods, Supplementary Information). The use of a PEAI solution treatment to form a 2D capping layer on top of the perovskite has been widely investigated, since a low dimensional perovskite capping layers passivates surface defects and the longer organic spaces in the 2D perovskites are able to reduce the water penetration and therefore improve the perovskite stability [13, 14, 44-48]. The Cl_6SubPc and C_{60} bilayer ETL was then thermally evaporated on top of the perovskites.

The performances of different devices are shown in **Fig. 1 c-h** and **Fig. S1-2**, and summarized in **Tables S1** and S**2.** The performance of 3D PVK devices for both ETLs is inferior to that of 3D/2D devices, in agreement with literature reports [14]. The 2D perovskite modification mainly contributed to the decrease in the trap density while maintain the electron mobility of the pure 3D perovskite, as demonstrated by the dark *J-V* characteristics of the electron only devices (see **Fig. S3**) [14].We also observe that CsFAMA 3D PVK devices with thin Cl_6SubPc (20 nm) ETLs exhibited a relatively low efficiency of 19.3%, due to the low J_{sc} and V_{oc}. This may arise from the mismatch

of the energy levels at the interface which hinders electron transfer, due to the relatively high LUMO level (~3.8 eV) of Cl_6SubPc [41]. The up-shift of the conduction band of 3D/2D PVK in comparison to 3D PVK (from ~4.0 eV to ~3.8 eV) [44] could enable improved electron collection and for the 3D/2D PVK/ Cl_6SubPc devices and thus an increase of the PCE to 20.5%. Similar improvements are seen for the 3D/2D PVK/C60 devices, where the efficiency increases from 20.2% to 20.8% (**Table S1**).

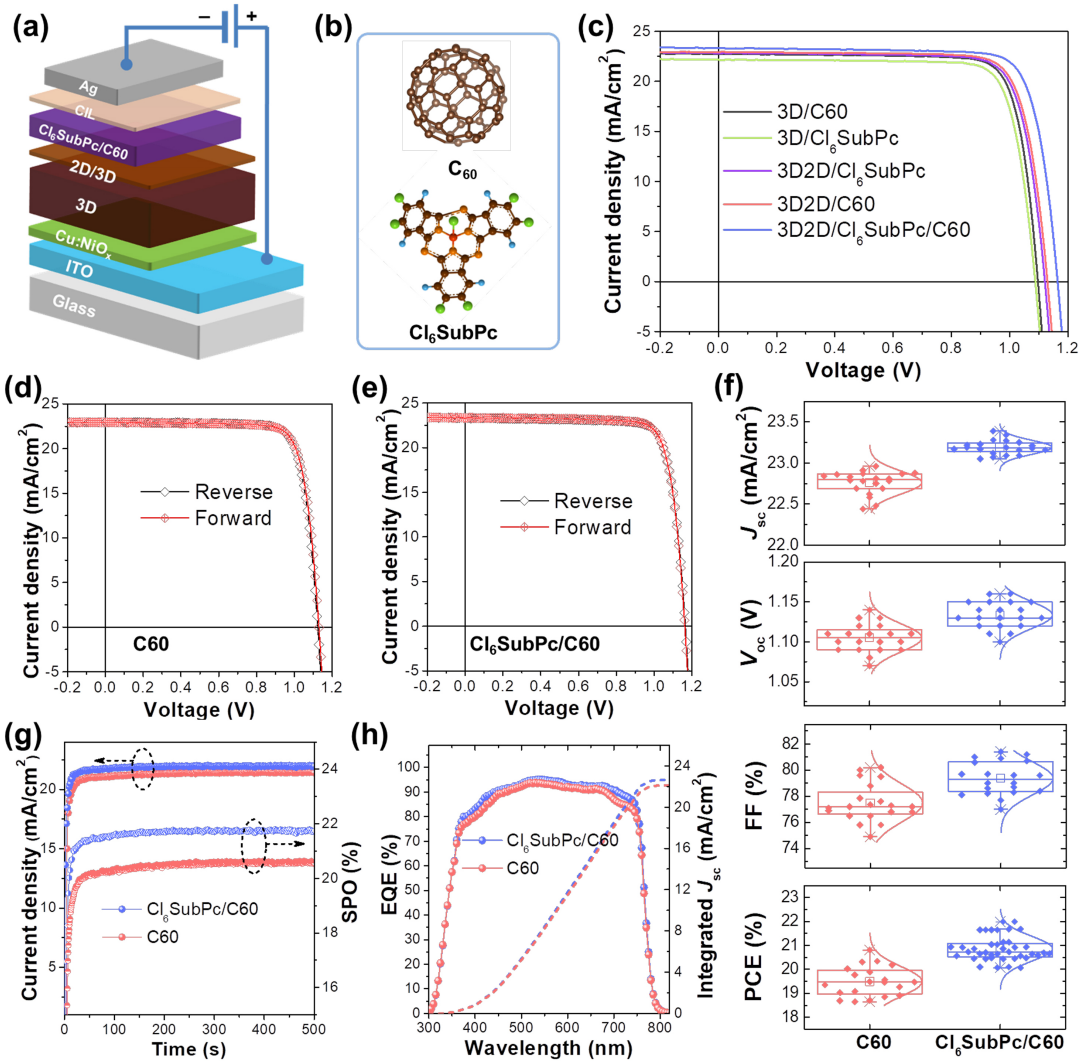

Fig. 1. (a) Device architecture of the inverted planar perovskite solar cells (PSCs); (b) Molecular structures of the C_{60} and chlorinated macrocyclic molecule (Cl_6SubPc) ETLs; (c) *J-V* curves of the PSCs with various ETLs (reverse scan) under 1 sun illumination; (d-e) *J-V* curves of the optimal 3D/2D/C60 (d) and

3D/2D/Cl_6SubPc/C60 (e) devices under reverse and forward scan directions; (f) Device performance statistics for 3D/2D/C_{60} and 3D/2D/Cl_6SubPc/C_{60} devices; (g) Steady power output (SPO) of the optimal 3D/2D/C_{60} and 3D/2D/Cl_6SubPc/C_{60} devices test at the bias of maximum power point; (h) EQE spectra for the optimal 3D/2D/C_{60} and 3D/2D/Cl_6SubPc/C_{60} devices.

Since non-fullerene ETLs offer a compromise between efficiency and stability when employed as interlayer between the perovskite and fullerene, we also investigated the performance of devices with Cl_6SubPc/C60 bilayer ETL for different Cl_6SubPc thicknesses, as shown in **Fig. S2**. For optimal Cl_6SubPc thickness of 8 nm, the PCE can be further improved to 22.0% (with a V_{oc} of 1.16 V, a J_{sc} of 23.31 mA/cm^2 and a high FF of 81.2 %) by using the 3D/2D PVK/ Cl_6SubPc/C60 (8/20 nm) structure, as shown in **Fig. 1c** and **Table S1**. Both devices with C60 and Cl_6SubPc/C60 ETLs show negligible I-V hysteresis (**Fig. 1d and 1e**). Significant improvements in the performance when using Cl_6SubPc are evident from the steady power output (**Fig. 1g**) and external quantum efficiency (EQE) curves (**Fig. 1f**), and the integrated J_{sc} values from EQE spectra are consistent with the I-V results. The statistical distribution of device performances is shown in **Fig. 1f**, and summarized in **Table S2**. The performance improvement after inserting thin layer of Cl_6SubPc may arise from the significant reduction in interfacial recombination losses due to the strong bonding effect of Cl_6SubPc molecule with perovskite and better interfacial energetic alignment, which will be discussed in more details later. To further verify the reliability of the device performance, a non-encapsulated device in air at 63% ambient humidity was certified at a PCE of 21.3% (The National Institute of Metrology (NIM), **Fig. S4**). This efficiency is among the best reported for *p-i-n* PSCs

(**Table S3**), and is the highest certified efficiency for planar inverted PSCs with inorganic HTLs. Furthermore, the devices with Cl_6SubPc/C60 ETL exhibited similar high performance with different electrodes, as shown in (**Fig. S5 and Table S4**), indicating the broad process window for our interfacial modification strategy.

3.2 Morphological, compositional and structural characterizations.

To understand the observed performance improvements, we performed comprehensive morphological, compositional and structural characterizations of the devices. From the SEM images and XRD patterns (**Fig. S6**), we observe an increase in grain size and a decrease of diffraction peak intensity of PbX_2 (PbI_2/$PbBr_2$) (~12.7°) in 3D/2D PVK samples. The impact of 2D capping layers and the additional Cl_6SubPc ETL on the perovskite morphology and crystallinity were investigated using grazing-incidence wide-angle X-ray scattering (GIWAXS). As shown in **Fig. S7**, an isotropic scattering profile (azimuthally uniform diffraction rings) at high q values ($q > 1$ Å^{-1}), indicate a random orientation of the crystal grains in 3D PVK films. After passivation with PEAI, we observe sharp Bragg diffraction spots in the out-of-plane (OOP) direction at low q values ($q < 0.9$ Å^{-1}), indicating the formation of 2D PVK oriented parallel to the surface of the 3D PVK surface (**Fig. S7 b-c**) [49, 50]. **Fig. S8 a-b** show that Cl_6SubPc is amorphous with no obvious diffraction features of Cl_6SubPc for the 3D/2D PVK/Cl_6SubPc sample. We note that the arc shape at q～0.9 Å^{-1} suggests a PbX_2 (PbI_2 and/or $PbBr_2$) residue. 1D azimuthal integrated scattering profiles are shown in **Fig. S9**. We can observe a decrease in PbX_2 content (peak ratios of signature peaks at q～0.91 Å^{-1} and q～1.0 Å^{-1} are assigned to the (001) plane of

PbX_2 crystal and (110) plane of 3D PVK) in 2D/3D PVK compared to 3D PVK. The improvement in crystallinity after PEAI treatment is in agreement with the surface induced secondary grain growth observed upon treating halide perovskite surfaces with organic ammonium solution [51]. Surprisingly, the deposition of Cl_6SubPc also induced further changes in the crystal structure. We observe reduced FWHMs (full width at half maximum) of the reflection at q ~ 0.28 $Å^{-1}$ and q ~ 0.38 $Å^{-1}$ (OOP) of the 2D perovskites Cl_6SubPc, increased ratio of the areas of the reflection at q ~ 0.77 $Å^{-1}$ for 2D PVSK to the reflection at q～1.0 $Å^{-1}$ for CsFAMA PVK, as well as reduced peaks of the hexagonal non-PVK phase (δ phase) at q ~ 0.85 $Å^{-1}$ (OOP) and PbX_2 at q ~ 0.91 $Å^{-1}$, indicating improved crystallinity. One possible mechanism behind the observed phenomenon is that Cl_6SubPc caused surface-induced secondary grain growth after the deposition of organic molecules on the surface of the perovskite to minimize the interfacial energy, facilitated by the low activation energies for ion diffusion, low elastic modulus and consequent liquid-like behavior of the soft perovskite lattice [51]. Even though the reasons for the observed changes after Cl_6SubPc deposition are not fully clear. However, it should be noted that recrystallization of the perovskite can not only be induced by organic ammonium molecule surface treatment, but also over time in the presence of strong chemical interactions with the electrode in HTL-free PSCs [31, 52]. To gain further insight into the structure of the films and possible effects of Cl_6SubPc, we performed cross-sectional cryogenic-transmission electron microscopy (cryo-TEM), as well as theoretical calculations of interactions between Cl_6SubPc and the perovskite.

Cryo-TEM images and the electron energy loss spectroscopy (EELS) mapping images are shown in **Fig. 2 a-g.** As shown in **Fig. 2b**, the higher magnification image of perovskites at the interface of ETL/PVK shows the surface layer of perovskite is composed of both 3D and 2D perovskites. The Fourier transformed electron diffraction (FTED) pattern from the high resolution transmission electron microscopy (HRTEM) image shows 3D CsFAMA PVK is a typical cubic phase with lattice parameters (a = b) of 3.2 Å (**Fig. 2c**), which is in agreement with the result of XRD patterns (**Fig. S6**) and similar to the previous reports of 3D PVK [53, 54]. Enlarged lattice of the $(110)_C$ plane can clearly distinguish the identical position of $[PbI_6]^{4-}$ octahedra and cations (**Fig. 2e**), which is also shown schematically for clear understanding. For 2D PVK shown in **Fig. 2d**, the lattice and FTED are different from that 3D PVK. Observed lattice distance of 7.1 Å corresponding to n=1 is consistent with the 0.88 $Å^{-1}$ peak in both in plane and out of plane patterns of the GIWAXS result discussed above and the previously reported value of PEA based 2D PVK.[35] The magnified lattice of 2D PVK also exhibits the obvious chains of $[PbI_6]^{4-}$ octahedra and PEA^+ included cations. Moreover, we found 2D PVK grains were dotted in the interfacial layer of PVK, which is out of our imagination that a 2D PVK thin layer with high orientation covers the surface of 3D PVK film. To the best knowledge of us, our work is the first time to discover the real microstructure of the device's cross-section via near atomic-scale HRTEM images, although that kind of HRTEM images of isolate PVK films were reported [54]. **Fig. 2g** shows the EELS element mapping of each key element involved in the ETL/PVK interface of a fresh

Cl_6SubPc/C60 bilayer ETL based 2D/3D PVK device. We can also observe that while there are clear boundaries between other layers in the device, Cl_6SubPc and C60 appear to be intermixed. The images obtained are consistent with STEM images and energy dispersive X-ray (EDX) mapping, **Fig. S10 and S11**.

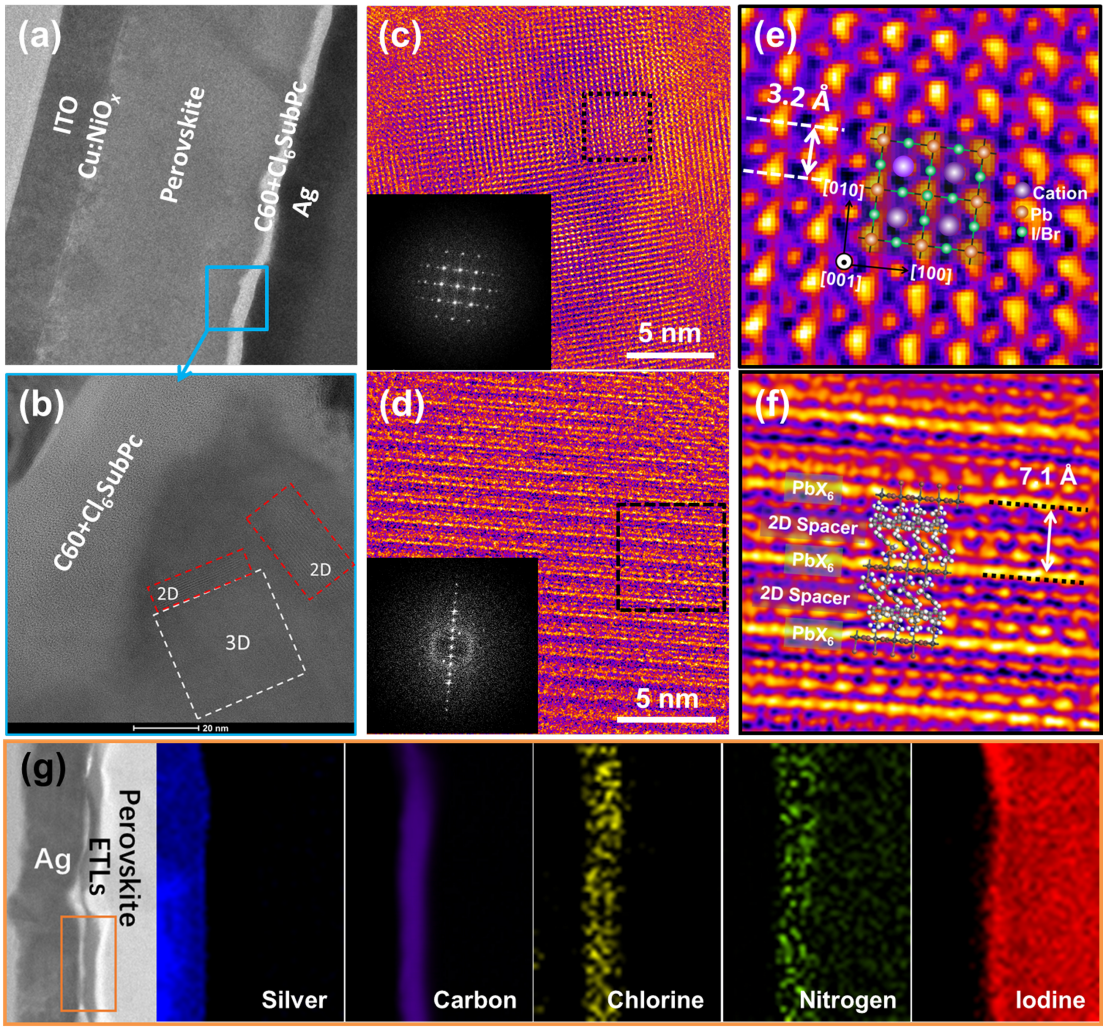

Fig. 2. (a) Cross sectional Cryo-transmission electron microscopy (TEM) image of a device with PEAI treated perovskite and Cl_6SubPc/C60 ETLs; (b) Cryo-TEM image of the enlarged area marked by blue frame in (a); (c) Cryo-HRTEM image of the 3D region marked in (b); (d) Cryo-HRTEM image of the 2D region marked in (b). Inserts in (c) and (d) are the corresponding fast Fourier transform (FFT) patterns; (e) Atomic-resolution TEM image of the marked area in (c), showing 3D crystal structure of the perovskite. The inserted structural model of typical cubic lattice well matches with the TEM image; (f) Atomic-resolution TEM image of the marked area in (d), showing clearly the layered structure of the 2D perovskite with interlayer distance of 7.1Å, which is consistent with the values from the single crystal structure; (g) Electron energy loss spectroscopy (EELS) mapping of the fresh devices with 3D/2D

perovskite and Cl_6SubPc/C60 ETLs. The Cl and N signal demonstrate that the Cl_6SubPc is mixed with the C60 film.

3.3 Theoretical calculation and analysis

The interactions between Cl_6SubPc and perovskite could be expected from findings in a previous report on the strong chemical interactions between the copper phthalocyanine and the perovskite [55], and are consistent with observed solar cell performance improvements and improved crystallinity. Possible mechanisms of defect passivation include the formation of Pb-Cl bonds [52], and the interaction between the perovskite and the pyrrole ring [55]. We investigated these possibilities using DFT and molecular dynamics simulations, as described in the experimental section. We found that two Cl ions bond to Pb in the PbI_2-terminated perovskite (001) in both possible adsorption configurations (**Fig. S12**) with a binding energy of -1.24 eV, which is much higher than the binding energy obtained for C_{60} (-0.11 eV). The experimentally observed downward shift in the energies of the XPS peaks of Pb after Cl_6SubPc deposition (**Fig. S13**) confirms the binding between the perovskite and Cl_6SubPc, in agreement with a previous report on the formation of Pb-Cl bond [52]. In addition, we calculated the H-bonding energies for PEA-PEA cations and Cl_6SubPc-PEA-Cl_6SubPc (see details in the experimental section) to be -0.013 eV and -0.035 eV, respectively. Thus, the use of Cl_6SubPc is expected to significantly increase the strength of interaction between the perovskite and ETL, due to hydrogen bonding (2.7 times stronger bonding with Cl_6SubPc compared to hydrogen bonding between PEA molecules), Pb-Cl interactions, and the strong bonding of iodine to Cl_6SubPc (more than 20 times stronger bonding with iodine compared to C_{60}). The

formation of strong bonds between the perovskite and charge transport layer are beneficial for device performance because they inhibit ion migration [56], and increase resistance to degradation due to oxygen and moisture [57]. In addition, the existence of strong interactions between the perovskite and interfacial layer on one side, and interfacial layer and fullerene derivative on the other side was found to result in defect passivation and substantial improvement in stability [58]. Interfacial bonding was confirmed to play a role in stability improvements for different molecules [56, 58], including copper phthalocyanine [56]. Thus, the stronger bonding achieved by using Cl_6SubPc interfacial layer can contribute to defect passivation [59] and to increase the device stability [56, 58].

3.4 Charge recombination dynamics and interfacial properties

Therefore, we performed comprehensive investigation of the effects of the incorporation of Cl_6SubPc on the charge recombination dynamics, the photoluminescence (PL) decay dynamics were measured to probe the interfacial recombination at the 3D/2D PVK/ETLs interfaces, followed by comprehensive stability testing. As shown in **Fig. 3 a-c,** the average lifetime (samples illuminated from perovskite side) of the PVK/Cl_6SubPc/C60 (626.3 ns) is similar to pure perovskites (723.5 ns), whereas the lifetime is dramatically reduced (105.9 ns) for perovskite/C60 films (**Table S5**). No obvious differences in τ_2 lifetime are found when the samples are illuminated from the glass side. Hence, the decrease of carrier lifetime when the sample is illuminated through the ETL surface arises from interfacial recombination at the PVK/ETL interface that can be suppressed by the

incorporation of Cl_6SubPc ETL between 3D/2D PVK and C60 [17]. Admittance spectroscopy was performed to determine the trap density of states (t-DOS) for the control and Cl_6SubPc devices [60]. The distribution is given as $DOS(E_\omega) = -\frac{V_{bi}}{qW}\frac{dC}{d\omega}\frac{\omega}{KT}$, where V_{bi}, W, C, ω, K, q and T are built-in potential, depletion width, capacitance, angular frequency, Boltzmann constant, elementary charge and temperature, respectively [61, 62]. V_{bi} can be obtained from the $1/C^2$–V Mott-Schottky plots shown in **Fig. S14**, where V_{bi} is given by the intersection on the bias axis [61]. The trap density (**Fig. 3e)** obtained is in the range expected for a polycrystalline halide perovskite film [62]. We observe a reduction in the trap state density for both trap states with depths ~0.30-0.42 eV and 0.50-0.60 eV in the Cl_6SubPc/C_{60} device in comparison to the C_{60} control one by approximately one order of magnitude (for example, from 1.53×10^{17} cm^{-3} eV^{-1} to 3.43×10^{16} cm^{-3} eV^{-1} for the trap state ~0.30-0.42 eV). We attribute these to the decrease of traps in grain boundaries and n-type interfaces, respectively, indicating that the PVK/ETL interface quality has a significant influence on the formation of defects in the planar PSCs. The dependence of the V_{oc} on light intensity is shown in **Fig. 3f**. The diode ideality factor (N_d) can be calculated from the V_{oc} dependence on illumination intensity [63]. N_d is reduced from 1.33 *KT/q* for the C_{60} ETLs device to 1.12 *KT/q* for the Cl_6SubPc/C60 device. A lower ideality factor indicates lower trap-assisted Shockley-Read-Hall monomolecular recombination [35, 64], which is consistent with the increased V_{oc} [3]. lower trap densities, and the suppression of interfacial recombination for devices with Cl_6SubPc/C60 ETLs. From the energy levels of different materials in the devices,

shown from the UPS profiles in **Fig. 3 d-e**, we can observe that the electron collection would be more favorable when using Cl_6SubPc/C60 ETLs, which likely accounts for observed higher efficiency of the devices containing Cl_6SubPc/C60 ETL compared to only C60 and Cl_6SubPc ETL. This has been further confirmed by the UPS depth profile of the 3D and 3D/2D perovskite films (**Fig. S15**).

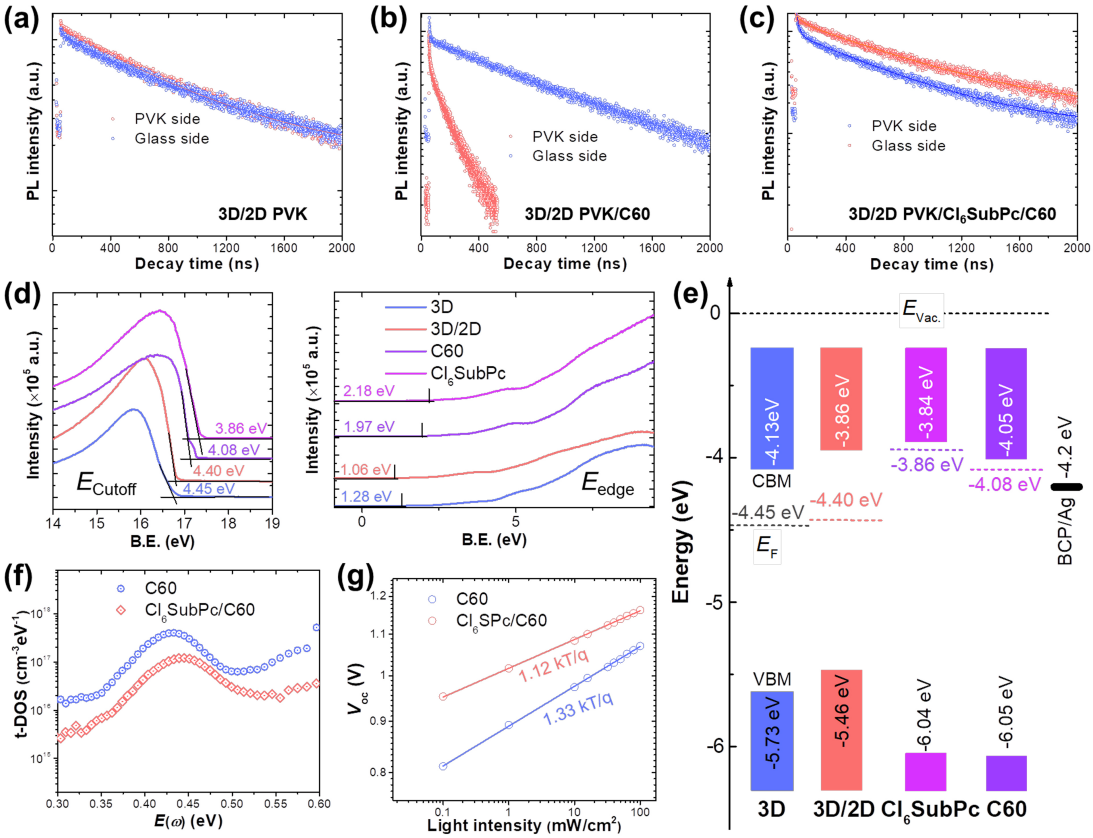

Fig. 3. (a-c) PL decay dynamics for the 3D/2D perovskites with different interlayers as noted in the Figures. The excitation from glass and perovskites sides were recorded for comparison. "PVK side" indicates the excitation is from perovskite side and "Glass side" means the excitation is from glass side. (d) UPS spectra for the 3D and 3D/2D perovskites as well as C60 and Cl_6SubPc ETLs prepared on Si substrates; (e) Energy level alignments of the various layers, the VBM, CBM and E_F values were calculated from the UPS results, data for BCP/Ag were cited from literature; (f) *t*-DOS characteristics for C60 control and Cl_6SubPc/C60 ETLs based PSCs; (g) Open circuit voltage (V_{oc}) as function of illumination intensity for the C60 control and Cl_6SubPc/C60 ETLs based PSCs.

3.5 Comprehensive device stability characteristics

After examining the charge recombination dynamics in detail, we performed comprehensive stability tests since interface degradation is a major contributor to the short and long-term PSC stability [65]. We performed stability tests in an inert environment to obtain information on the intrinsic stability independent of the encapsulant used. During continuous one-sun illumination, 95% of the initial PCE is retained after 1200 hours, as shown in **Fig. 4a** (corresponding time dependences of V_{oc}, J_{sc}, and FF are shown in **Fig. S16**). During storage in an inert atmosphere for over 7000 hours, devices with 3D/2D perovskite passivation and Cl_6SubPc/C60 ETLs maintained 99% of the initial performance, a significant improvement over devices with pure C60 ETLs, as shown in **Fig. S17**. The devices with Cl_6SubPc/C60 ETLs also showed superior thermal stability with only a ~5% degradation after 2000 hours at 80 ºC in a N_2 filled glove box, compared to ~25% obtained for devices without Cl_6SubPc, as shown in **Fig. S4b** (corresponding time dependences of V_{oc}, J_{sc}, and FF are shown in **Fig. S18**). In addition to the stability testing in inert environment, additional tests were conducted at ambient and a high temperature, high humidity (85ºC, 85% RH) environment, using encapsulated devices (schematic diagrams are shown in **Fig. S19** and **20**). We also observe a superior performance in damp heat test, where devices with Cl_6SubPc/C60 ETLs exhibit T_{80} of 816 h (34 days), while devices with C60 ETLs drop below 80% of initial efficiency within the first day of testing, as shown in **Fig. 4c.** We also performed outdoor testing since outdoor stability studies of PSCs in general have been scarce [66], and there have been no outdoor tests of inverted devices to date. Superior stability of the devices with Cl_6SubPc/C60 ETLs

compared to C60 ETLs is also confirmed in outdoor stability tests following ISOS-O1 protocol, where T_{95} of 1272h for device with Cl_6SubPc is obtained, as shown in **Fig. 4d**. The encapsulated cell with Cl_6SubPc/C60 ETL exhibited excellent stability in ambient under simulated solar illumination and MPP tracking, as shown in **Fig. 4e.**

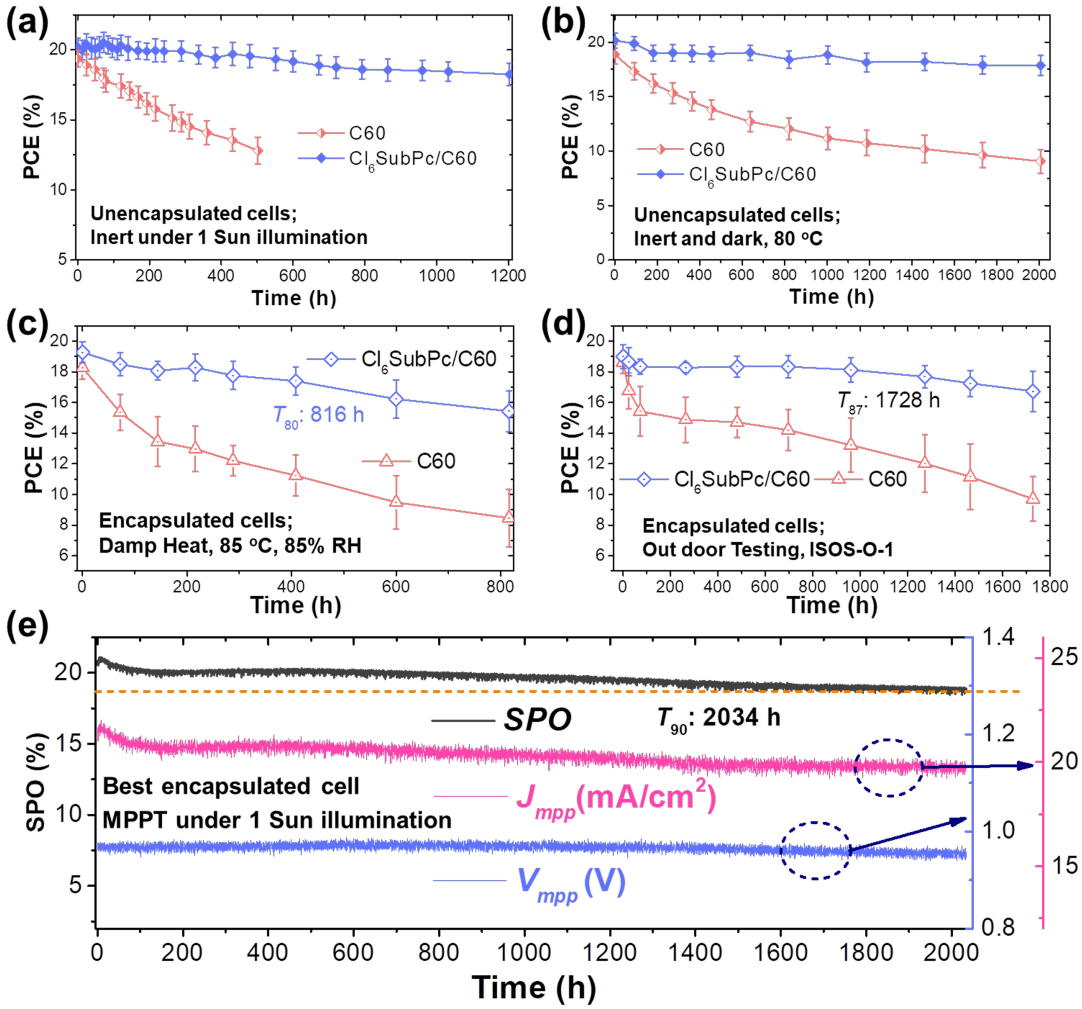

Fig. 4. (a) Light stability tests of the control C60 devices (6 cells) and Cl_6SubPc/C60 devices (6 cells) in inert atmosphere. The devices were un-encapsulated, and the I-V cures were recorded at certain time intervals; (b) Thermal stability tests of the control C60 devices (6 cells) and Cl_6SubPc/C60 devices (8 cells) at 80 °C under inert and dark environment; (c) Damp heat stability tests of the encapsulated control C60 devices (5 cells) and Cl_6SubPc/C60 devices (5 cells); (d) Outdoor stability tests of the encapsulated control C60 devices (5 cells) and Cl_6SubPc/C60 devices (9 cells) following the ISOS-O-1 protocol standard; (e) Light stability of encapsulated Cl_6SubPc/C60 cell in ambient under continuous 1 sun illumination and maximum power point tracking (MPPT).

It should be noted that all the stability tests were performed on devices with 3D/2D PVK layers. Since it has been reported that bulky organic cations in the 2D PVK structure of the 3D/2D PVK capping layers improves device stability by inhibiting ion migration [5, 47, 67, 68], we also compared the stability of devices with 3D and 3D/2D PVK and C60 ETL, as shown in **Fig. S21**. Thus, we can observe that while 3D/2D PVK results in improved stability compared to 3D PVK active layer, as expected [47, 67, 68], it is not sufficient to enable significant performance improvement under realistic operating conditions. From the comparison of the stability of the devices with 3D PVK active layer and Cl_6SubPc/C60 and C60-only ETLs, as shown in **Fig. S22**. We see that the stability of the devices with 3D PVK and Cl_6SubPc/C60 is clearly better than that of 3D PVK and C60-only. Thus, we focus on the effect of the PVK/ETL interface on device stability in devices with 3D/2D perovskite and Cl_6SubPc/C60 bilayer ETL.

In addition to stability tests at elevated temperature, humidity and/or illumination, we performed stability testing under reverse bias, since this type of test is a strong indicator of susceptibility to ion migration and electrode corrosion [31, 69]. To further enhance susceptibility to ion migration, the devices were illuminated during testing, since illumination and electrical bias both promote ion and defect migration, and accelerate harmful chemical reactions [66]. In the device without Cl_6SubPc (**Fig. S23**) we can see clear damage to the Ag electrode, and also Ag deposition on the ITO side, in agreement with the literature [69], while in the devices with Cl_6SubPc/C60 (**Fig. S24**) no obvious electrode damage can be seen, confirming further that Cl_6SubPc is

capable of blocking ion migration.

3.6 Analysis of the possible mechanisms of improved device stability

To investigate the mechanism behind the effect of Cl_6SubPc in device stability tested above, we performed ToF-SIMS, EELS mapping, and XPS measurements on devices with different ETLs. From obtained SIMS profiles (**Fig. 5a** and **b**, and **Fig. S25**) of the C60-only and Cl_6SubPc/C60 devices before and after aging, we observe the iodine at the initial sputtering atmosphere of the aged C60-only device in contrast to the fresh one, along with the variation of silver information. In contrast, the Cl_6SubPc/C60 device shows negligible change in those profiles. Information on other key elements or species involved in the devices before and after aging is also shown in **Fig. S25.** To verify the profiles obtained from SIMS and provide direct visual evidence of ion migration, we have applied our successful experience of sample preparation and HRTEM-characterization of the intact device cross-section, and obtained visual EELS mappings of involved key elements of fresh and aged devices. **Fig. 5c-d** show the EELS mappings of the aged device cross-sections of the C60-only and Cl_6SubPc/C60 device, compared with those of the corresponding fresh one (**Fig. 2g** and **Fig. S26**). The iodine mapping in the aged C60-only device proves unambiguously the existence of iodide inside the silver electrode, while the counterpart iodine mapping in the aged Cl_6SubPc/C60 device shows negligible existence of iodine in the corresponding silver electrode layer. This contrast reveals in a direct view the effect of Cl_6SubPc to block the migration of iodine ions although that is well known already.

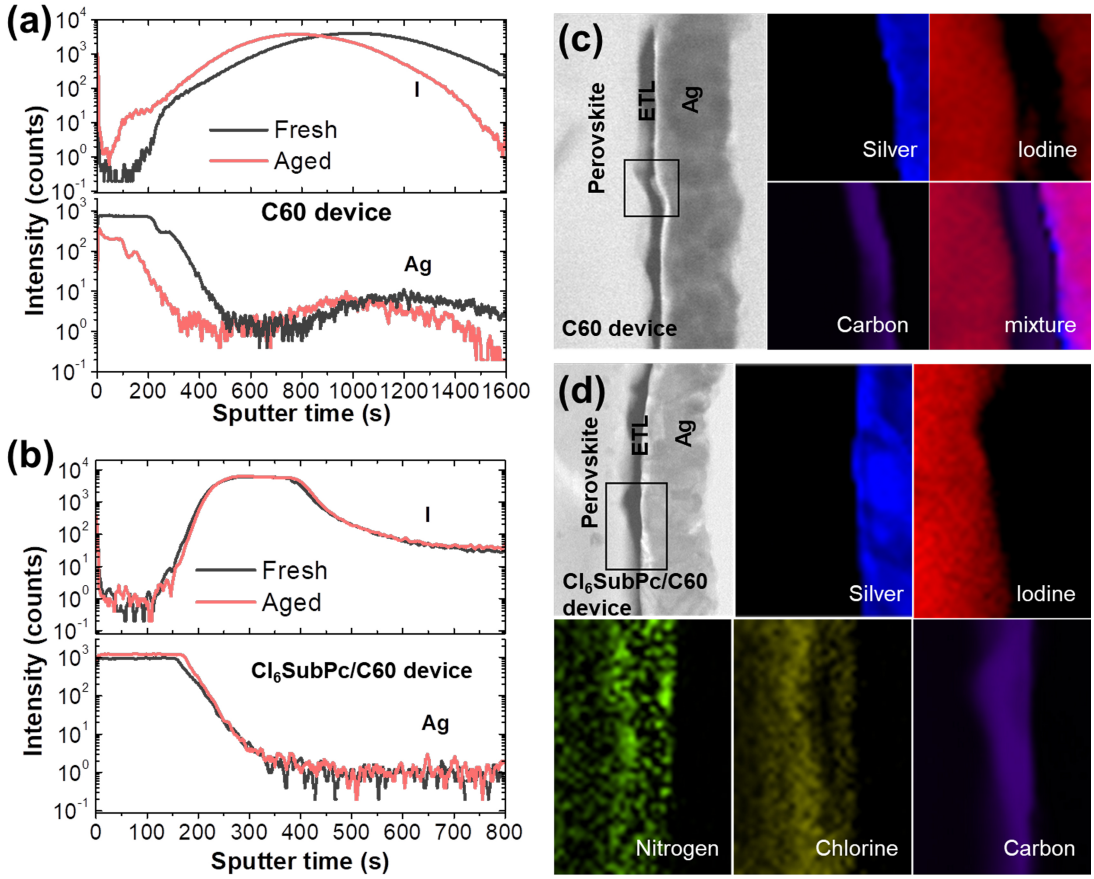

Fig. 5. (a) and (b) Secondary-ion mass spectrometry (SIMS) profiles of I^- and Ag^+ ions for the C60 control device (a) and Cl_6SubPc/C60 device (b) before and after aging; (c) and (d) lateral EELS mapping of the aged C60 control device (c) and Cl_6SubPc/C60 (d) device.

Moreover, in agreement with the SIMS and EELS mapping results, XPS spectra of the devices with Cl_6SubPc/C60 ETL do not show significant changes in the I and Ag spectra after aging, different from devices with C60 ETLs, as shown in **Fig. S27**. Surface potential scans probed by scanning Kelvin probe microscopy (SKPM) further highlight the differences in the stability of the PVK/ETL interface with and without Cl_6SubPc (**Fig. S28** and **S29).** The surface potential for the perovskite with Cl_6SubPc/C60 ETLs, showed no obvious changes as function of illumination (continuous light soaking with a white LED lamp, ~40 mA/cm^2) (**Fig. S29**), while perceptible changes have been observed in the C60-only sample (**Fig. S28**). The

demonstrated improvement in the device stability and the stability of the Cl_6SubPc/PVK interface that hinders the ion migration is in agreement with the calculated binding energy for iodine ions (-0.43 eV for Cl_6SubPc and -0.019 eV for C60), since the binding energy increase would stabilize the PVK/ETL interface.

To further investigate the reason of the blocking effect of Cl_6SubPc, XPS spectra of Cl_6SubPc film treated with iodide vapor were measured, as shown in **Fig. S30.** The I^- signal can be detected in the treated film and the binding energy of N 1s core was shifted to a lower energy, indicating a strong interaction between N and I [70]. The N in the Cl_6SubPc contributes to I^- adsorption, which suppresses ion migration in the PVK/ETL interface. This is in agreement with the known capability of macrocyclic molecules (porphyrins, phthalocyanines) to effectively adsorb iodine [71], as well as the high iodide ion binding energy of the Cl_6SubPc. In addition to interactions between N and I, boron atom can also contribute to the interactions with the perovskite, since we observed an obvious red shift of the binding energy of B1s from 191 to 186 eV, as shown in **Fig. S31b**. This shift is consistent with electron transfer, which likely occurs due to high electron affinity of boron, similar to a previous report of electron transfer between SubPc and C60, which also resulted in a similar shift of the B 1s peak [72]. Consequently, Cl_6SubPc strongly interacts with both perovskite, as evidenced by XPS results shown in **Fig. S31**, and C60 based on literature reports [72], and this can contribute to the stabilization of the interface [56, 58] as well as improved charge collection [73]. It should be noted that this electron transfer can result in the possible loss of axial chlorine, which could then diffuse into the

perovskite layer and hence be detected in the perovskite layer after aging, as shown in EELS mapping images, **Fig. 5d.** That may also correlate to a small shift in Cl profile in the SIMS profiles (**Fig. S25**). As discussed above, the synergistic effect of N, B and Cl elements of Cl_6SubPc accounts for the correlated chemical bonding with both PVK and C60, leading to the effective suppression of ions migration at the interface.

Finally, to examine the validity and general applicability of phthalocyanine molecule structure in enhancing device stability, a typical electron-transport molecule, F_{16}CuPc whose structure is shown in **Fig. S32a**, was tested as a replacement for Cl_6SubPc in device structure. The devices with F_{16}CuPc/C60 ETLs exhibit much lower efficiency of 16.39%, as shown in **Fig. S32b**. The inferior performance compared to Cl_6SubPc/C60 devices can be attributed to unfavorable energy level alignment, as shown in **Fig. S33**, and consistent with the observed lower FF (due to the increase of series resistance), which indicates less efficient charge collection. In contrast to the control C60-only device, the devices with F_{16}CuPc/C60 still exhibit superior stability under illumination and MPPT (**Fig. S34**), as well as reverse bias and illumination (**Fig. S35**), similar as the devices with Cl_6SubPc/C60 ETL. This result further demonstrates that the phthalocyanines can effectively interact with iodine and the perovskite and thus inhibit the ion migration.

4. Conclusions

In summary, we have shown that the Cl_6SubPc/C60 combined ETL can dramatically boost the device stability, as well as improve the conversion efficiency owing to the unique properties of Cl_6SubPc. Based on comprehensive experimental

characterizations and theoretical simulations, N and B atoms of Cl_6SubPc could have obvious chemical bonding with migrated halide ions from perovskites, which in addition to Pb-Cl bonds results in strong interactions between the ETL and perovskite, resulting in effective inhibition of the halide ion migration at the ETL/PVK interface and the suppression of electrode corrosion, as evidenced by EELS mapping, TOF-SIMS, and XPS. As a result of effective interfacial management strategy, we obtained inverted planar PSCs with high conversion efficiency of 22 % (21.3% certified) and unprecedented long-term stability (95% of PCE retained over 1200h of outdoor testing and 90% of PCE retained under illumination and MPPT for over 2000 h). This strategy can be extended to extensive phthalocyanines with suitable electronic structures for interfacial stabilization of PSCs. Our results highlight multilayer ETLs incorporating halogenated macrocyclic molecules as a promising route for both high performance and stable perovskite solar cells.

Conflict of interest

The authors declare that they have no conflict of interest.

Acknowledgements

This work is supported by the National Natural Science Foundation of China (NSFC) (Nos. 61775091, U2001216), the Shenzhen Key Laboratory Project (No. ZDSYS201602261933302) and Natural Science Foundation of Shenzhen Innovation Committee (No. JCYJ20180504165851864). A. B. D. would like to acknowledge support of Seed Funding for Basic Research and Seed Funding for Strategic Interdisciplinary Research Scheme of the University of Hong Kong and Shenzhen Science and Technology Commission Projects No. JCYJ20170818141216288. The authors thank the Core Research Facilities (CRF) and the Pico Center of SUSTech for some characterizations in this work. Q. H. and T. P. R. were supported by the US

Office of Naval Research under contract N00014-17-1-2241. GIXD were performed at beamline 7.3.3 at Advanced Light Source, Lawrence Berkeley National Laboratory, which was supported by the DOE, Office of Science, and Office of Basic Energy Sciences.

Author contributions

Zhubing He conceived and supervised the project. Wei Chen, Qin Hu, Rui Zhu, Thomas P. Russell, Aleksandra B. Djurišić and Zhubing He wrote the paper. Wei Chen fabricated and characterized the perovskite solar cells. Bin Han, Yudong Zhu, Wei Chen and Meng Gu finished the FIB, STEM, EELS and HRTEM characteristics and analysis. Qin Hu and Wenqiang Yang performed GIWAXS measurements and analyzed the GIWAXS data. Rui Cheng and Shien Ping Feng helped perform damp heat stability tests. Yecheng Zhou performed the theoretical calculation and analyzed the results. Deying Luo and Fangzhou Liu helped perform all other related characterizatons and measurements. All authors discussed and analyzed the results.

Appendix A. Supplementary material

Supplementary materials to this article can be found online at https://xxxx.

References

[1] Park N-G, Grätzel M, Miyasaka T, et al. Towards stable and commercially available perovskite solar cells. Nat Energy 2016; 1: 16152.

[2] Rong Y, Hu Y, Mei A, et al. Challenges for commercializing perovskite solar cells. Science 2018; 361: eaat8235.

[3] Luo D, Yang W, Wang Z, et al. Enhanced photovoltage for inverted planar heterojunction perovskite solar cells. Science 2018; 360: 1442-1446.

[4] Liu M, Johnston MB, Snaith HJ. Efficient planar heterojunction perovskite solar cells by vapour deposition. Nature 2013; 501: 395-398.

[5] Boyd CC, Cheacharoen R, Leijtens T, et al. Understanding degradation mechanisms and improving stability of perovskite photovoltaics. Chem Rev

2019; 119: 3418-3451.

[6] Zhao X, Kim HS, Seo JY, et al. Effect of selective contacts on the thermal stability of perovskite solar cells. ACS Appl Mater Interfaces 2017; 9: 7148-7153.

[7] Wang Q, Phung N, Di Girolamo D, et al. Enhancement in lifespan of halide perovskite solar cells. Energy Environ Sci 2019; 12: 865-886.

[8] Bai S, Da P, Li C, et al. Planar perovskite solar cells with long-term stability using ionic liquid additives. Nature 2019; 571: 245-250.

[9] Islam MB, Yanagida M, Shirai Y, et al. Highly stable semi-transparent mapbi3 perovskite solar cells with operational output for 4000 h. Sol Energy Mater Sol Cells 2019; 195: 323-329.

[10] Cheacharoen R, Rolston N, Harwood D, et al. Design and understanding of encapsulated perovskite solar cells to withstand temperature cycling. Energy Environ Sci 2018; 11: 144-150.

[11] Tan H, Jain A, Voznyy O, et al. Efficient and stable solution-processed planar perovskite solar cells via contact passivation. Science 2017; 355: 722-726.

[12] Hou Y, Du X, Scheiner S, et al. A generic interface to reduce the efficiency-stability-cost gap of perovskite solar cells. Science 2017; 358: 1192-1197.

[13] Jiang Q, Zhao Y, Zhang X, et al. Surface passivation of perovskite film for efficient solar cells. Nat Photonics 2019; 13: 460-466.

[14] Jung EH, Jeon NJ, Park EY, et al. Efficient, stable and scalable perovskite solar cells using poly(3-hexylthiophene). Nature 2019; 567: 511-515.

[15] Saliba M, Matsui T, Domanski K, et al. Incorporation of rubidium cations into perovskite solar cells improves photovoltaic performance. Science 2016; 354: 206-209.

[16] Wu WQ, Yang Z, Rudd PN, et al. Bilateral alkylamine for suppressing charge recombination and improving stability in blade-coated perovskite solar cells. Sci Adv 2019; 5: eaav8925.

[17] Stolterfoht M, Wolff CM, Marquez JA, et al. Visualization and suppression of

interfacial recombination for high-efficiency large-area pin perovskite solar cells. Nat Energy 2018; 3: 847-854.

[18] Lian J, Lu B, Niu F, et al. Electron-transport materials in perovskite solar cells. Small Methods 2018; 2: 1800082.

[19] Tress W. Perovskite solar cells on the way to their radiative efficiency limit - insights into a success story of high open-circuit voltage and low recombination. Adv Energy Mater 2017; 7: 1602358.

[20] Hu Q, Chen W, Yang W, et al. Improving efficiency and stability of perovskite solar cells enabled by a near-infrared-absorbing moisture barrier. Joule 2020; 4: 1575-1593.

[21] Akbulatov AF, Frolova LA, Griffin MP, et al. Effect of electron-transport material on light-induced degradation of inverted planar junction perovskite solar cells. Adv Energy Mater 2017; 7: 1700476.

[22] Yang D, Zhou X, Yang R, et al. Surface optimization to eliminate hysteresis for record efficiency planar perovskite solar cells. Energy Environ Sci 2016; 9: 3071-3078.

[23] Yang D, Yang R, Ren X, et al. Hysteresis-suppressed high-efficiency flexible perovskite solar cells using solid-state ionic-liquids for effective electron transport. Adv Mater 2016; 28: 5206-5213.

[24] Yang D, Yang R, Wang K, et al. High efficiency planar-type perovskite solar cells with negligible hysteresis using edta-complexed SnO_2. Nat Commun 2018; 9: 3239.

[25] Chen W, Zhou Y, Chen G, et al. Alkali chlorides for the suppression of the interfacial recombination in inverted planar perovskite solar cells. Adv Energy Mater 2019; 9: 1803872.

[26] Xue QF, Bai Y, Liu MY, et al. Dual interfacial modifications enable high performance semitransparent perovskite solar cells with large open circuit voltage and fill factor. Adv Energy Mater 2017; 7: 1602333.

[27] Li Z, Jo BH, Hwang SJ, et al. Bifacial passivation of organic hole transport interlayer for niox-based p-i-n perovskite solar cells. Adv Sci 2019; 6: 1802163.

[28] Deng YH, Zheng XP, Bai Y, et al. Surfactant-controlled ink drying enables high-speed deposition of perovskite films for efficient photovoltaic modules. Nat Energy 2018; 3: 560-566.

[29] Shao Y, Yuan Y, Huang J. Correlation of energy disorder and open-circuit voltage in hybrid perovskite solar cells. Nat Energy 2016; 1: 15001.

[30] Yao K, Leng S, Liu Z, et al. Fullerene-anchored core-shell zno nanoparticles for efficient and stable dual-sensitized perovskite solar cells. Joule 2019; 3: 417-431.

[31] Yang S, Chen S, Mosconi E, et al. Stabilizing halide perovskite surfaces for solar cell operation with wide-bandgap lead oxysalts. Science 2019; 365: 473-478.

[32] Huang Z, Hu X, Liu C, et al. Nucleation and crystallization control via polyurethane to enhance the bendability of perovskite solar cells with excellent device performance. Adv Funct Mater 2017; 27: 1703061.

[33] Chen W, Xu L, Feng X, et al. Metal acetylacetonate series in interface engineering for full low-temperature-processed, high-performance, and stable planar perovskite solar cells with conversion efficiency over 16% on 1 cm^2 scale. Adv Mater 2017; 29: 1603923.

[34] Chen W, Wu Y, Fan J, et al. Understanding the doping effect on nio: Toward high-performance inverted perovskite solar cells. Adv Energy Mater 2018; 8: 1703519.

[35] Chen W, Zhou Y, Wang L, et al. Molecule-doped nickel oxide: Verified charge transfer and planar inverted mixed cation perovskite solar cell. Adv Mater 2018; 30: 1800515.

[36] Dong Q, Liu F, Wong MK, et al. Encapsulation of perovskite solar cells for high humidity conditions. Chemsuschem 2016; 9: 2597-2603.

[37] Zhou Y, Long G. Low density of conduction and valence band states contribute to the high open-circuit voltage in perovskite solar cells. J Phys Chem C 2017; 121: 1455-1462.

[38] Kresse G, Furthmüller J. Comput Mater Sci 1996; 6: 15.

[39] Kresse G, Furthmüller J. Phys Rev B 1996; 54: 11169.

[40] Urbani M, de la Torre G, Nazeeruddin MK, et al. Phthalocyanines and

porphyrinoid analogues as hole- and electron-transporting materials for perovskite solar cells. Chem Soc Rev 2019;

[41] Duan C, Zango G, Garcia Iglesias M, et al. The role of the axial substituent in subphthalocyanine acceptors for bulk-heterojunction solar cells. Angew Chem Int Ed 2017; 56: 148-152.

[42] Li H, Ding X, Han B-H. Porous azo-bridged porphyrin-phthalocyanine network with high iodine capture capability. Chem-Eur J 2016; 22: 11863-11868.

[43] Saliba M, Matsui T, Seo JY, et al. Cesium-containing triple cation perovskite solar cells: Improved stability, reproducibility and high efficiency. Energy Environ Sci 2016; 9: 1989-1997.

[44] Bai Y, Xiao S, Hu C, et al. Dimensional engineering of a graded 3d-2d halide perovskite interface enables ultrahigh v_{oc} enhanced stability in the p-i-n photovoltaics. Adv Energy Mater 2017; 7: 1701038.

[45] Gharibzadeh S, Abdollahi Nejand B, Jakoby M, et al. Record open‐circuit voltage wide‐bandgap perovskite solar cells utilizing 2d/3d perovskite heterostructure. Adv Energy Mater 2019; 1803699.

[46] Chen P, Bai Y, Wang SC, et al. In situ growth of 2d perovskite capping layer for stable and efficient perovskite solar cells. Adv Funct Mater 2018; 28: 1706923.

[47] Grancini G, Roldan-Carmona C, Zimmermann I, et al. One-year stable perovskite solar cells by 2d/3d interface engineering. Nat Commun 2017; 8: 15684.

[48] Lee JW, Dai Z, Han TH, et al. 2d perovskite stabilized phase-pure formamidinium perovskite solar cells. Nat Commun 2018; 9: 3021.

[49] Quan LN, Yuan M, Comin R, et al. Ligand-stabilized reduced-dimensionality perovskites. J Am Chem Soc 2016; 138: 2649-2655.

[50] Quintero-Bermudez R, Gold-Parker A, Proppe AH, et al. Compositional and orientational control in metal halide perovskites of reduced dimensionality. Nat Mater 2018; 17: 900-907.

[51] Xue J, Wang R, Wang K-L, et al. Crystalline liquid-like behavior: Surface-induced secondary grain growth of photovoltaic perovskite thin film. J

Am Chem Soc 2019; 141: 13948-13953.

[52] Wang Y, Wu T, Barbaud J, et al. Stabilizing heterostructures of soft perovskite semiconductors. Science 2019; 365: 687-691.

[53] Lee J-W, Dai Z, Han T-H, et al. 2d perovskite stabilized phase-pure formamidinium perovskite solar cells. Nat Commun 2018; 9: 3021.

[54] Zhu Y, Gui Z, Wang Q, et al. Direct atomic scale characterization of the surface structure and planar defects in the organic-inorganic hybrid ch3nh3pbi3 by cryo-tem. Nano Energy 2020; 73: 104820.

[55] Kim YC, Yang TY, Jeon NJ, et al. Engineering interface structures between lead halide perovskite and copper phthalocyanine for efficient and stable perovskite solar cells. Energy Environ Sci 2017; 10: 2109-2116.

[56] Roose B, Wang Q, Abate A. The role of charge selective contacts in perovskite solar cell stability. Adv Energy Mater 2018; 9: 1803140.

[57] Xing G, Mathews N, Sun S, et al. Long-range balanced electron- and hole-transport lengths in organic-inorganic $ch_3nh_3pbi_3$. Science 2013; 342: 344-347.

[58] Luo B, Yao Y, Tian E, et al. Interfacial bonding and electronic structure between copper thiocyanate and hybrid organohalide lead perovskites for photovoltaic application. J Phys Chem Lett 2019; 10: 5609-5616.

[59] Heo JH, Lee S-C, Jung S-K, et al. Efficient and thermally stable inverted perovskite solar cells by introduction of non-fullerene electron transporting materials. J Mater Chem A 2017; 5: 20615-20622.

[60] Wang Q, Shao Y, Dong Q, et al. Large fill-factor bilayer iodine perovskite solar cells fabricated by a low-temperature solution-process. Energy Environ Sci 2014; 7: 2359.

[61] Laban WA, Etgar L. Depleted hole conductor-free lead halide iodide heterojunction solar cells. Energy Environ Sci 2013; 6: 3249.

[62] Shao Y, Xiao Z, Bi C, et al. Origin and elimination of photocurrent hysteresis by fullerene passivation in $ch_3nh_3pbi_3$ planar heterojunction solar cells. Nat Commun 2014; 5: 5784.

[63] Tress W, Yavari M, Domanski K, et al. Interpretation and evolution of open-circuit voltage, recombination, ideality factor and subgap defect states during reversible light-soaking and irreversible degradation of perovskite solar cells. Energy Environ Sci 2018; 11: 151-165.

[64] Li Z, Zhang C, Shao Z, et al. Controlled surface decomposition derived passivation and energy-level alignment behaviors for high performance perovskite solar cells. J Mater Chem A 2018; 6: 9397-9401.

[65] Brinkmann KO, Zhao J, Pourdavoud N, et al. Suppressed decomposition of organometal halide perovskites by impermeable electron-extraction layers in inverted solar cells. Nat Commun 2017; 8: 13938.

[66] Khenkin MV, Katz EA, Abate A, et al. Consensus statement for stability assessment and reporting for perovskite photovoltaics based on isos procedures. Nat Energy 2020; 5: 35-49.

[67] Bai S, Da P, Li C, et al. Planar perovskite solar cells with long-term stability using ionic liquid additives. Nature 2019; 571: 245-250.

[68] Chen P, Bai Y, Wang S, et al. In situ growth of 2d perovskite capping layer for stable and efficient perovskite solar cells. Adv Funct Mater 2018; 28: 1706923.

[69] Razera RAZ, Jacobs DA, Fu F, et al. Instability of p–i–n perovskite solar cells under reverse bias. J Mater Chem A 2020; 8: 242-250.

[70] Back H, Kim G, Kim J, et al. Achieving long-term stable perovskite solar cells via ion neutralization. Energy Environ Sci 2016; 9: 1258-1263.

[71] Li H, Ding X, Han B-H. Porous azo-bridged porphyrin–phthalocyanine network with high iodine capture capability. 2016; 22: 11863-11868.

[72] Lo M-F, Ng T-W, Mo H-W, et al. Suppression of time-dependent donor/acceptor interface degradation by redistributing donor charge density. Adv Mater Interfaces 2014; 1: 1300082.

[73] Zou M, Xia X, Jiang Y, et al. Strengthened perovskite/fullerene interface enhances efficiency and stability of inverted planar perovskite solar cells via a tetrafluoroterephthalic acid interlayer. ACS Appl Mater Interfaces 2019; 11: 33515-33524.